Systematic Method for the Kinetic Modeling of Temporally Resolved Hyperspectral Microscope Images of Fluorescently Labeled Cells

PATRICK J. CUTLER, DAVID M. HAALAND, and PAUL J. GEMPERLINE*

Department of Chemistry, East Carolina University, Greenville, North Carolina 27858 (P.J.C., P.J.G.); and Sandia National Laboratories, Albuquerque, New Mexico 87185-0895 (D.M.H.)

In this paper we report the application of a novel method for fitting kinetic models to temporally resolved hyperspectral images of fluorescently labeled cells to mathematically resolve pure-component spatial images, pure-component spectra, and pure-component reaction profiles. The method is demonstrated on one simulated image and two experimental cell images, including human embryonic kidney cells (HEK 293) and human A549 pulmonary type II epithelial cells. In both cell images, inhibitor kappa B kinase alpha (IKKα) and mitochondrial antiviral signaling protein (MAVS) were labeled with green and yellow fluorescent protein, respectively. Kinetic modeling was performed on the compressed images by using a separable least squares method. A combination of several first-order decays were needed to adequately model the photobleaching processes for each fluorophore observed in these images, consistent with the hypothesis that each fluorophore was found in several different environments within the cells. Numerous plausible mechanisms for kinetic modeling of the photobleaching processes in these images were tested and a method for selecting the most parsimonious and statistically sufficient model was used to prepare spatial maps of each fluorophore.

Index Headings: **Hyperspectral confocal microscopy; Fluorescence imaging; Kinetic modeling; Human embryonic kidney cells; Human A549 pulmonary type II epithelial cells; Inhibitor kappa B kinase alpha; Mitochondrial antiviral signaling protein; Separable least squares.**

INTRODUCTION

The development of new technologies provides the opportunity to collect larger and ever more complex data sets. These new forms of data facilitate the study of more intricate systems and the development of new methods for obtaining valuable information from these complex data sets. Advances in detectors and other such technologies have brought about a renaissance in fluorescence microscopy.[1,2] Our hyperspectral confocal fluorescence microscope can be used to acquire spatial and temporal hyperspectral images with diffraction-limited resolution.[3] The images produced by this instrument are capable of resolving multiple fluorophores with high spectral and spatial overlap when analyzed with multivariate curve resolution (MCR) techniques.[4,5] The analysis of temporally resolved hyperspectral microscope fluorescence images provides the opportunity to follow biochemical processes at a subcellular level as a function of time. This investigation is focused on developing and applying new methods for the kinetic modeling of these temporal hyperspectral fluorescence images.

Fluorescent proteins are frequently used to label proteins *in vivo* to study protein expression and to monitor their spatial locations in the cell.[6] It is often advantageous to observe several fluorescently labeled proteins simultaneously. Due to high spectral overlap of the emission spectra of some fluorescent proteins, filter-based microscopes are limited in the number and specific combinations of fluorescent proteins that can be observed simultaneously. This limitation can be overcome by obtaining hyperspectral microscope images that are analyzed with MCR techniques.[3]

To develop the use of kinetic modeling in the investigation of temporally resolved hyperspectral images of fluorescently labeled cells, we initially focused on the modeling of the kinetic process of photobleaching of multiple fluorescing species in the cells. A key problem with performing kinetic modeling on a hyperspectral fluorescence image is that the concentrations of all modeled species at time zero (t_0) are unknown. In typical multivariate kinetic modeling algorithms, the initial concentrations of all species must be known;[7–9] therefore, a recently developed kinetic modeling approach based on separable least squares[10] (SLS) has been extended and implemented in this investigation. Note that although this approach has only been applied in this investigation to systems undergoing photobleaching, the approach is general and can be applied to any multivariate kinetic data that follow a first-order reaction.

Kinetic modeling can be performed on several multivariate data sets simultaneously,[11–13] but due to memory and time constraints there are limitations to the number of multivariate data sets that can be analyzed simultaneously. A typical temporal hyperspectral microscope image acquired by our instrument has the dimensions 200 pixels by 200 pixels by 512 wavelengths by 18 time slices, producing about 3 GB worth of data when represented as 8 bytes per point. In this scheme, a complete multivariate spectroscopic data set measured as a function of time is acquired for each pixel. For an image of 200 $\times$ 200 pixels, there are 40000 pixels and thus 40000

Received 3 November 2008; accepted 29 December 2008.
* Author to whom correspondence should be sent. E-mail: gemperlinep@ecu.edu.

0003-7028/09/6303-0261$2.00/0
© 2009 Society for Applied Spectroscopy

multivariate data sets that can be analyzed simultaneously, one for each pixel. Due to memory and time limitations, it is not practical to analyze all 40000 temporally resolved multivariate data sets simultaneously with our current kinetic modeling approach. Therefore, we compress the data to a manageable size while retaining a maximal amount of useful and diverse information. Intelligent pixel selection and signal averaging are used to compress the hyperspectral confocal images to a manageable size in this investigation.

A systematic approach to the kinetic modeling of temporally resolved hyperspectral microscope fluorescence images has been developed in this work. The main steps in this systematic approach are (1) preprocessing the data, (2) data compression, (3) kinetic modeling of the compressed image, (4) model selection, and (5) projection of the compressed image back to the full image. Describing this systematic approach and its application to several temporally resolved hyperspectral fluorescence images of fixed fluorescently labeled cells is the main focus of this manuscript.

THEORY

In order to minimize computation times and memory utilization for the kinetic modeling of the hyperspectral image data, spatial data compression is implemented. The compressed data is then kinetically modeled using a technique based on the separable least squares (SLS) algorithm previously reported.[10] An extension of this SLS technique, which incorporates several first-order decays for each fluorescent specie in the image, has been implemented in this work.

Spatial Image Compression. The spatial compression of temporally resolved hyperspectral image data is performed using the initial time slice. The steps developed in this work for spatial compression include (1) thresholding the image, (2) selection of a key set of maximally dissimilar spectra,[14] and (3) subsequent averaging of spectra found to be similar to the key set of spectra.

Image Thresholding. An estimate of the signal-to-noise ratio (S/N) is used to threshold the hyperspectral image data. The preprocessed spectra (see Experimental section) in each pixel of the initial time slice are filtered using a three-point binomial smoothing filter.[15] The residuals between the smoothed and preprocessed spectra are calculated for each pixel. The S/N of each pixel is estimated by dividing the mean of the preprocessed spectra for each pixel by the standard deviation in the residuals for each pixel. The S/N threshold was empirically determined and set to 1.3. All pixels with S/N above 1.3 are retained and pixels equal to or below are discarded.

Selection of a Key Set of Maximally Dissimilar Spectra. Key set factor analysis is a method for selecting a set of rows (or columns) in a data set that are most orthogonal to each other. This method was initially proposed and demonstrated by Malinowski[16] who later refined this method into iterative key set factor analysis.[14] Our selection of a key set of maximally dissimilar spectra (pixels) is based on this iterative key set factor analysis.

The first time slice from the temporal hyperspectral image is used for the selection of a key set of maximally dissimilar spectra. The initial step is to perform principal component analysis[17] (PCA) reconstruction to improve the signal-to-noise for the spectra in the first temporal slice. The spectra are compressed to $k + 1$ principal components, where k is the number of apparent principal components. The number of principal components, k, is determined by inspection of a scree plot, shapes of loading vectors, and PCA of spectral residuals. The PCA compressed spectra are then used for the remaining steps in the selection of a key set of maximally dissimilar spectra. It is important to use information from PCA when selecting the size of the key set of maximally dissimilar spectra. If the size of the key set of maximally dissimilar spectra exceeds the number of apparent principal components, then some of the spectra selected by the process presented here will most likely be noisy, low intensity spectra.

An initial key spectrum, $\mathbf{s}_{p1}$, is selected as the most intense spectrum that has the maximum difference from the mean spectrum. The next step is to select a spectrum from the remaining set of spectra that is maximally dissimilar from $\mathbf{s}_{p1}$. To perform this task $(m - 1)$ 2-by-2 pair-wise variance-covariance matrices are computed between $\mathbf{s}_{p1}$ and all other PCA compressed spectra in the first time slice. Equations 1 and 2 show the general form for the variance-covariance matrix, $\mathbf{\Sigma}$, for m spectra:

$$\sigma_{i,j}^2 = \frac{1}{n-1}\sum_{k=1}^{n}(s_{k,i} - \bar{s}_i)(s_{k,j} - \bar{s}_j) \tag{1}$$

$$\Sigma_{s_1,s_2,\ldots,s_m} = \begin{bmatrix} \sigma_{1,1}^2 & \sigma_{1,2}^2 & \cdots & \sigma_{1,m}^2 \\ \sigma_{2,1}^2 & \sigma_{2,2}^2 & \cdots & \vdots \\ \cdots & \cdots & \ddots & \vdots \\ \sigma_{m,1}^2 & \sigma_{m,2}^2 & \cdots & \sigma_{m,m}^2 \end{bmatrix} \tag{2}$$

where $\mathbf{s}_{k,i}$ is the kth response from the ith spectrum and n is the number of response measurements acquired per spectrum.

The determinant is computed for each of the $(m - 1)$ variance-covariance matrices, and the spectrum, $\mathbf{s}_{p2}$, that corresponds to the largest absolute value of the determinants is added to the key set. This process yields the pair of spectra that are the most orthogonal. Subsequent spectra are added to the key set by the step-wise selection of the next spectrum that yields the maximum determinant of the variance-covariance matrix for an increasing number of spectra until the desired number of spectra $\mathbf{s}_{p1}, \mathbf{s}_{p2}, \ldots, \mathbf{s}_{pi}$ are selected. The number of key spectra selected is equal to the number of PCA components required to represent the data down to the noise level. This initial key set sometimes needs refinement, as spectra selected early in the sequential process may have unintended correlations to spectra selected later in the process.

The key set of spectra is then refined by performing a step-wise replacement of each key spectrum $\mathbf{s}_{p1}, \mathbf{s}_{p2}, \ldots, \mathbf{s}_{pi}$ with spectra found to further maximize the determinant of the corresponding variance-covariance matrix. This process is repeated until the key set of selected spectra remains constant through an entire cycle of the step-wise replacement process. The resultant spectra are the key set of maximally dissimilar spectra.

Selection of Maximally Dissimilar Regions and Averaging. Maximally dissimilar regions are computed by finding the 100 spectra best correlated to each spectrum in the key set of maximally dissimilar spectra. The maximally dissimilar regions are averaged into super pixels. All pixels above the S/N threshold but not included in the sets of maximally dissimilar regions are averaged into an additional super pixel. This

additional super pixel is included in order to ensure that low intensity signals in the background are included in the spatially compressed image so that it accurately represents the full image.

Extension of Separable Least Squares. Kinetic modeling using separable least squares (SLS) is based on the separation of linear parameters such as the concentrations at time zero (t_0) from the set of nonlinear parameters (rate constants) describing the change in concentration over time.[10] This approach of separating linear and nonlinear parameters is only applicable to kinetic mechanisms of first-order reactions.[10] In this work, the SLS approach is specifically applied to the mechanism of first-order decay. The set of basis functions, **F**, that describe the temporal change in concentration for the mechanism of first-order decay for z species are computed using Eq. 3:

$$\mathbf{F}_{(m\times z)} = [e^{-tk_1}|e^{-tk_2}|\cdots|e^{-tk_z}] \tag{3}$$

where t is time and k_z is the rate constant for the zth specie.

A brief discussion of the data organization methods and the underlying concepts employed in this algorithm is necessary in order to describe the extension of the SLS method utilized in this investigation. The linear additive model for the spectral image data is expressed in Eq. 4:

$$\mathbf{D}^i_{(m\times n)} = \mathbf{C}^i_{(m\times z)}\mathbf{S}^{\mathrm{T}}_{(z\times n)} + \mathbf{E}^i_{(m\times n)} \tag{4}$$

where $\mathbf{D}^i$ is the set of temporally resolved spectra in the ith spatial pixel in the image (m time-resolved spectra by n spectral wavelengths), $\mathbf{C}^i$ is the matrix of temporally resolved concentration profiles for the z fluorophores in the ith pixel, **S** is the matrix of resolved pure-component spectral responses, and $\mathbf{E}^i$ is an error matrix for the ith pixel. The entire set of temporally resolved spectra in the ith spatial pixel, $\mathbf{D}^i$, is represented as a column vector, $d^i_{vec(m\cdot n\times 1)}$, using Eq. 5:

$$\mathbf{d}^i_{vec} = vec(\mathbf{D}^i) \tag{5}$$

where $vec(\mathbf{X})$ transforms **X** into $\mathbf{x}_{vec}$ with one column stacked onto the next. The set of z basis functions, **F**, describing the temporal change in concentrations are combined with the z pure-component spectral responses at the jth wavelength, $\mathbf{s}_j$, to form $\mathbf{\Phi}_j$ as shown in Eq. 6:

$$\mathbf{\Phi}_j = \mathbf{F}\, diag(\mathbf{s}_{j,}) \tag{6}$$

where $diag(\mathbf{x})$ transforms **x** into a square matrix with **x** along the diagonal and zeros elsewhere. The set of basis functions combined with the pure-component spectral responses for all n spectral wavelengths can be augmented to formulate $\mathbf{\Phi}_{\mathrm{stack}}$ shown in Eq. 7:

$$\mathbf{\Phi}_{\mathrm{stack}} = \left[\mathbf{\Phi}_1^{\mathrm{T}}|\mathbf{\Phi}_2^{\mathrm{T}}|\cdots|\mathbf{\Phi}_n^{\mathrm{T}}\right]^{\mathrm{T}} \tag{7}$$

The standard linear additive model can easily be expanded to describe all i spatial pixels simultaneously as shown in Eq. 8:

$$\left[(\mathbf{D}^1)^{\mathrm{T}}|(\mathbf{D}^2)^{\mathrm{T}}|\cdots|(\mathbf{D}^i)^{\mathrm{T}}\right]^{\mathrm{T}} = \left[(\mathbf{C}^1)^{\mathrm{T}}|(\mathbf{C}^2)^{\mathrm{T}}|\cdots|(\mathbf{C}^i)^{\mathrm{T}}\right]^{\mathrm{T}}\mathbf{S}^{\mathrm{T}} \tag{8}$$

where $\mathbf{D}^i$ is the set of temporally resolved spectra at spatial pixel i, and $\mathbf{C}^i$ represents the corresponding set of z temporally resolved concentration profiles. Similarly, the set of i vectorized temporally resolved spectra, $[\mathbf{d}^1_{vec}\,|\,\mathbf{d}^2_{vec}\,|\cdots|\,\mathbf{d}^i_{vec}]$, can be represented by $\mathbf{\Phi}_{\mathrm{stack}}$ (described in Eq. 7) and the matrix of concentrations at time t_0, $\mathbf{C}_0$. This relationship is shown in Eq. 9:

$$\left[\mathbf{d}^1_{vec}|\mathbf{d}^2_{vec}|\cdots|\mathbf{d}^i_{vec}\right]_{(m\cdot n\times i)} = \mathbf{\Phi}_{\mathrm{stack}(m\cdot n\times z)}\mathbf{C}_{0(z\times i)} + [\mathbf{e}^1_{vec}|\mathbf{e}^2_{vec}|\cdots|\mathbf{e}^i_{vec}] \tag{9}$$

In $\mathbf{C}_0$, the rows correspond to the number of fluorophores, z, in the system and the columns correspond to the i spatial pixels being analyzed. As described in the previously reported implementation of the SLS algorithm,[10] the linear parameters (concentrations of all fluorophores at t_0) for i multivariate data sets are estimated by performing the linear least squares step in Eq. 10 while the nonlinear parameters (rate constants) are estimated using a nonlinear least squares method.

$$\hat{\mathbf{C}}_0 = \mathbf{\Phi}^+_{\mathrm{stack}}\left[\mathbf{d}^1_{vec}|\mathbf{d}^2_{vec}|\cdots|\mathbf{d}^i_{vec}\right] \tag{10}$$

In Eq. 10, the $\hat{\mathbf{C}}_0$ indicates the least squares estimate and $^+$ represents the pseudo inverse of the matrix. As in the previous work, we use a fast combinatorial nonnegative least squares (fc-nnls) algorithm to solve Eq. 10.[18]

In the extension of the SLS algorithm presented here, several first-order decays are needed to describe the temporal changes in concentration of each fluorophore. For the photobleaching experiments modeled in this investigation, we hypothesize that each fluorophore can exist in multiple environments with indistinguishable spectral responses, each of which decays by a different first-order process to yield invisible (bleached) species. Consider the following two-component example for fluorophore A and B. A mechanism can be postulated with u first-order decays

$$A_1 \xrightarrow{k_{A1}} A_{b(1)}, A_2 \xrightarrow{k_{A2}} A_{b(2)}, \cdots, A_u \xrightarrow{k_{Au}} A_{b(u)},$$

describing fluorophore A and v first-order decays and

$$B_1 \xrightarrow{k_{B1}} B_{b(1)}, B_2 \xrightarrow{k_{B2}} B_{b(2)}, \cdots, B_v \xrightarrow{k_{Bv}} B_{b(v)},$$

describing fluorophore B such that the total number of species $z = u + v$.

An algorithmic approach to fitting the kinetic mechanism proposed above to i temporally resolved pixels is now described. Random numbers uniformly distributed on the interval 0 to 1 were used as initial estimates of the model parameters, which are rate constants ($k_{A1}, k_{A2}, \ldots, k_{Au}$ and $k_{B1}, k_{B2}, \ldots, k_{Bv}$) and concentrations $\mathbf{C}_{0(z\times i)}$ at t_0 for each pixel in the image. Using these inputs, several initialization steps are necessary prior to model optimization. As shown in Eq. 11, the initial parameter estimates for specie A_1 are used to construct temporal concentration profiles, $\mathbf{C}^{A_1}$ where $\mathbf{c}_0(A_1)$ is the corresponding row from $\mathbf{C}_{0(z\times i)}$.

$$\mathbf{C}^{A_1}_{(m\times i)} = e^{-\mathbf{t}k_{A1}}\mathbf{c}_0(A_1) \tag{11}$$

Temporally resolved concentration profiles $\mathbf{C}^{A_1}, \mathbf{C}^{A_2}, \ldots, \mathbf{C}^{A_u}$ and $\mathbf{C}^{B_1}, \mathbf{C}^{B_2}, \ldots, \mathbf{C}^{B_v}$ are constructed for each specie in this manner. The overall temporally resolved concentration profile for each fluorophore in each pixel is simply the sum of the profiles for each sub-specie in Eq. 12:

$$\mathbf{C}^A = \mathbf{C}^{A_1} + \mathbf{C}^{A_2} + \cdots + \mathbf{C}^{A_u} \tag{12}$$

The ith column of $\mathbf{C}^A$ is represented as $\mathbf{c}_i^A$, which is the temporally resolved concentration profile for specie A in the ith pixel. The matrix of concentrations, $\mathbf{C}^A$, is represented as a column vector, $\mathbf{c}_{vec}^A$ using Eq. 13:

$$\mathbf{c}_{vec}^A = vec(\mathbf{C}^A) \tag{13}$$

and the same procedure can be used to represent $\mathbf{C}^B$ as a column vector, $\mathbf{c}_{vec}^B$. The matrix of concentration profiles, $\mathbf{C}^{\text{Total}}$, which corresponds to $[(\mathbf{C}^1)^{\text{T}} \,|\, (\mathbf{C}^2)^{\text{T}} \,|\, \cdots \,|\, (\mathbf{C}^i)^{\text{T}}]^{\text{T}}$ in Eq. 8, is then formulated using Eq. 14:

$$\mathbf{C}_{(m\times 2)}^{\text{Total}} = [\mathbf{c}_{vec}^A | \mathbf{c}_{vec}^B] \tag{14}$$

Given the relationship in Eq. 8, the pure-component spectra, $\mathbf{S}$, are determined using the linear least squares step in Eq. 15:

$$\hat{\mathbf{S}}^{\text{T}} = (\mathbf{C}^{\text{Total}})^{+} \left[\mathbf{D}^1 | \mathbf{D}^2 | \cdots | \mathbf{D}^i\right]^{\text{T}} \tag{15}$$

Again the fc-nnls algorithm is used to implement nonegativity constraints in performing this linear least-squares step.[18] For the example mechanism described above, the kinetic analysis gives the pure-component spectra shown in Eq. 16 in which $\mathbf{s}_A$ is the spectral contribution from A and $\mathbf{s}_B$ is the spectral contribution from B.

$$\mathbf{S}_{(n\times 2)} = [\mathbf{s}_A | \mathbf{s}_B] \tag{16}$$

This last step concludes the initialization process for the SLS algorithm, and the optimization procedure follows.

The estimated pure-component spectra and initially estimated rate constants are used in the subsequent optimization steps. The basis functions ($\mathbf{F}$) are constructed using the estimated rate constants and Eq. 3, giving the functions shown in Eq. 17:

$$\mathbf{F}_{(n\times z)} = [e^{-tk_{A1}} | e^{-tk_{A2}} | \cdots | e^{-tk_{Au}} | e^{-tk_{B1}} | e^{-tk_{B2}} | \cdots | e^{-tk_{Bv}}] \tag{17}$$

where $e^{-tk_{A1}}$ produces the column vector describing the temporal changes in concentration for specie A_1, $e^{-tk_{A2}}$ produces the column vector describing the temporal changes in concentration for specie A_2, and so forth. The matrix $\mathbf{S}$ shown in Eq. 16 is expanded to Eq. 18 in order to correspond to the set of basis functions proposed by the mechanism:

$$\mathbf{S}_{\text{expand}(n\times z)} = [\mathbf{s}_A | \mathbf{s}_A | \cdots | \mathbf{s}_A | \mathbf{s}_B | \mathbf{s}_B | \cdots | \mathbf{s}_B] \tag{18}$$

$\mathbf{F}$ and $\mathbf{S}_{\text{expand}}$ defined in Eqs. 17 and 18, respectively, are used in Eqs. 6 and 7 to formulate $\mathbf{\Phi}_{\text{tack}}$, which is subsequently used in Eq. 10 to solve for the linear parameters, $\mathbf{C}_0$. Equations 11 through 14 are used to formulate $\mathbf{C}^{\text{Total}}$, which is used in Eq. 15 to update $\mathbf{S}$. The pure-component spectra, $\mathbf{S}$, are then normalized to unit length at each cycle of the iteration, and the concentration profiles, $\mathbf{C}^{\text{Total}}$, are subsequently scaled using the inverse of the spectral normalization constant. The nonlinear parameters, k_z, are subsequently estimated by using a nonlinear least-squares solver to minimize the residuals shown in Eq. 19, where $\mathbf{C}^{\text{Total}}$ is a function of rate constants k_z:

$$\left| \left[(\mathbf{D}^1)^{\text{T}} | (\mathbf{D}^2)^{\text{T}} | \cdots | (\mathbf{D}^i)^{\text{T}}\right]^{\text{T}} - \mathbf{C}^{\text{Total}}\mathbf{S}^{\text{T}} \right| \tag{19}$$

Several of the equations and steps in this section have been expressed using an example mechanism with two components, A and B, but the basic concepts in these equations and steps apply to more general first-order kinetic mechanisms. In the kinetic fitting process, all rate constants can be optimized or a subset of the rate constants can be optimized while others are held constant. In many of the mechanisms proposed and tested in this work, the rate constants for several species are constrained to equal zero. This constraint assumes that the fluorophore is present in an environment that undergoes an undetectable amount of photobleaching during the exposure time of the experiment. This is just one example of a mechanism that can be fit using the SLS algorithm, and its use is further discussed in later sections.

Environment 1	Environment 2	Environment 3
$YFP_1 \xrightarrow{k_1} YFP_{b(1)}$	$YFP_2 \xrightarrow{k_4} YFP_{b(2)}$	$YFP_0 \xrightarrow{k_7=0} YFP_0$
$GFP_1 \xrightarrow{k_2} GFP_{b(1)}$	$GFP_2 \xrightarrow{k_5} GFP_{b(2)}$	$GFP_0 \xrightarrow{k_8=0} GFP_0$
$Auto_1 \xrightarrow{k_3} Auto_{b(1)}$	$Auto_2 \xrightarrow{k_6} Auto_{b(2)}$	$Auto_0 \xrightarrow{k_9=0} Auto_0$

FIG. 1. In this proposed kinetic mechanism, each fluorophore YFP, GFP, and autofluorescence (Auto) can exist in up to three different environments. The fluorophores readily undergo photobleaching by first-order decays of differing rate constants in the first two environments while the fluorophores in the third environment experience negligible photobleaching during the time of the experiment, i.e., rates are 0. At least a single first-order decay is necessary to adequately model each fluorophore, yielding 64 possible variants of different combinations of fluorophores and environments.

EXPERIMENTAL

Cell Sample Preparation. The first sample that was imaged in this investigation consisted of human embryonic kidney cells (HEK 293) that were grown on No. 1.5 microscope cover slips (0.017 mm thick) to a density of 50%. The cells were then transiently transfected with plasmids expressing fluorescence-fusion proteins. The proteins, inhibitor kappa B kinase alpha (IKKα) and mitochondrial antiviral signaling protein (MAVS), were labeled with enhanced green fluorescent protein (GFP) and enhanced yellow fluorescent protein (YFP), respectively, using standard protocols with Lipofectamine 2000 reagent.[19] The cells were then fixed in a 3.7% paraformaldehyde solution of phosphate buffered saline (PBS) at room temperature for 15 minutes. After fixation, the cells were rinsed three times with PBS and air dried. The cover slip with the cells was then mounted on the microscope slide with DAKO fluorescent mounting medium. The temporally resolved hyperspectral image (18 repeated 2D image scans) of this sample will be referred to as Image 1.

The second sample that was imaged consisted of human A549 pulmonary type II epithelial cells. These cells were transiently transfected using the Amaxa Biosystems Nucleofector I according to the manufacturer's instructions.[20] As in the first sample, GFP labeled the IKKα protein and YFP was attached to the MAVS protein. In this case, the transient transfection was performed in solution and the transfected cells were then plated onto No. 1.5 cover slips. The cells were washed three times with PBS and then fixed at room temperature for 15 minutes in a PBS solution containing 3.6% paraformaldehyde with 5% sucrose added. The fixed sample was then washed three times with PBS, dried, and then mounted to the microscope slide with permafluor. The temporally resolved hyperspectral image of this sample (18 repeated 2D image scans) will be referred to as Image 2.

Simulated Image. A noise-free simulated image was constructed from the pure-component spectra, initial concentrations, and the reaction mechanism and similar rates obtained from the analysis of Image 1 (see Results Section and Fig. 2b). Poisson and read noise of the hyperspectral confocal fluorescence microscope was added to the noise-free simulated image to produce the final simulated image. The percent error in rate constants in Eq. 20 is the figure of merit used to compare a model estimated rate constant, $\hat{k}$, with the true value, k:

$$\text{rate constant } (\% \text{ error}) = 100 \times \left[\frac{(k-\hat{k})^2}{k^2}\right]^{1/2} \tag{20}$$

The spectral lack of fit (LOF) described in Eq. 21 is used to compare a model-estimated pure-component spectrum, $\hat{\mathbf{s}}$, with the true spectrum, $\mathbf{s}$:

$$\% \text{ LOF} = 100 \times \left[\frac{\sum_{j=1}^{n}(s_j - \hat{s}_j)^2}{\sum_{i=1}^{n} s_j^2}\right]^{1/2} \tag{21}$$

The accuracy of the estimated concentrations for a given chemical species, $\hat{c}_i$, is compared to the true concentrations, c_i, using the mean average deviation shown in Eq. 22 where n is the number of pixels:

$$\text{mean average deviation} = \frac{\sum_{i=1}^{n}|c_i - \hat{c}_i|}{n} \tag{22}$$

Image Acquisition. The hyperspectral confocal fluorescence microscope developed at Sandia National Laboratories[3] was use to acquire all images in this investigation. Image 1 was acquired using the 20×, NA 0.75 plan apochromat objective (Nikon) with a 0.5 nm x-step and 0.48 nm y-step size. Image 2 was acquired using the 60×, NA 1.4 apochromat objective (Nikon) with a 0.26 nm x-step and 0.24 nm y-step size. Several preprocessing steps are necessary after data acquisition. The image and dark current data are despiked to remove cosmic spikes. Detector offsets are first accounted for by subtracting the first eigenvector corresponding to the scores of the despiked dark image from the original despiked image. Any remaining detector offset is estimated by averaging data points 5–15 where no light reaches the detector, and this average offset is subtracted from the preprocessed spectra.[21]

RESULTS AND DISCUSSION

The two experimental temporally resolved hyperspectral images and the simulated image were modeled using the systematic kinetic modeling approach developed in this work. The systematic approach developed here consists of (1) spectral preprocessing steps; (2) data compression including thresholding, selecting maximally dissimilar regions, and pixel averaging; (3) kinetic modeling of multiple plausible mechanisms; (4) selection of the most parsimonious and statistically sufficient model; and (5) extrapolation from the compressed image back to the full image.

The preprocessing and image compression steps have been discussed above under the headings "Spatial image compression" and "Image acquisition", respectively. The resulting spatially compressed image is kinetically modeled with several plausible mechanisms using the extended SLS method discussed above. After sample treatment and preliminary

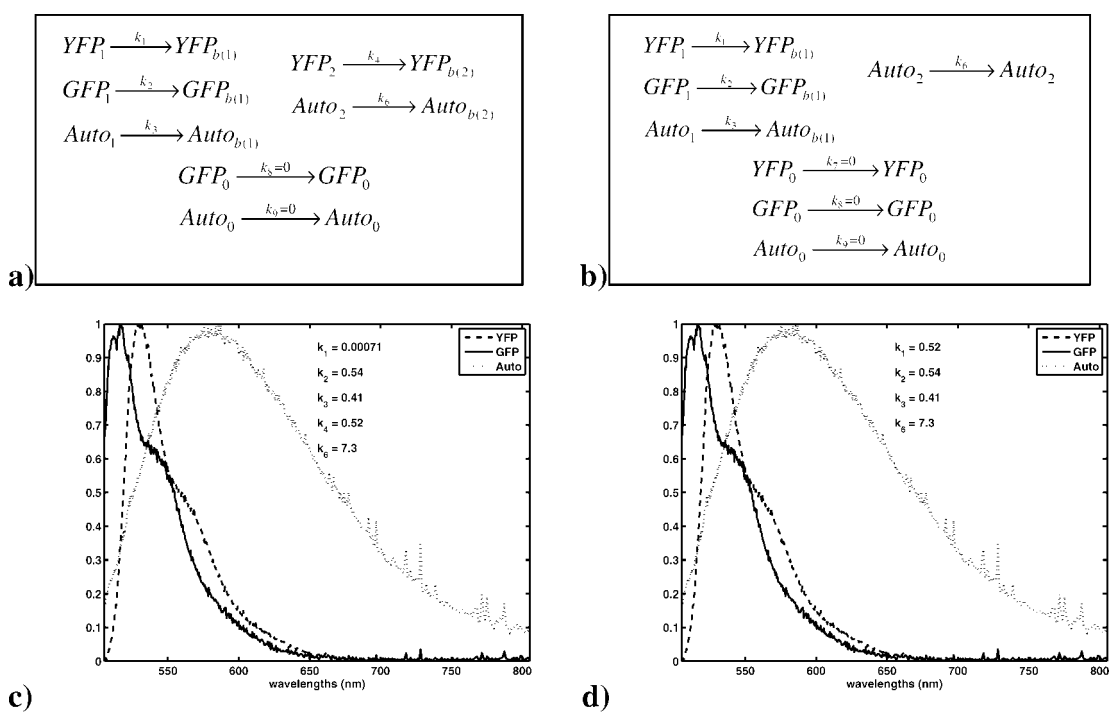

FIG. 2. Results from the kinetic modeling of a simulated image. (**a**) and (**b**) are proposed mechanisms, and their respective kinetic modeling results are shown in (**c**) and (**d**). The results from the kinetic modeling of these mechanisms are mathematically indistinguishable.

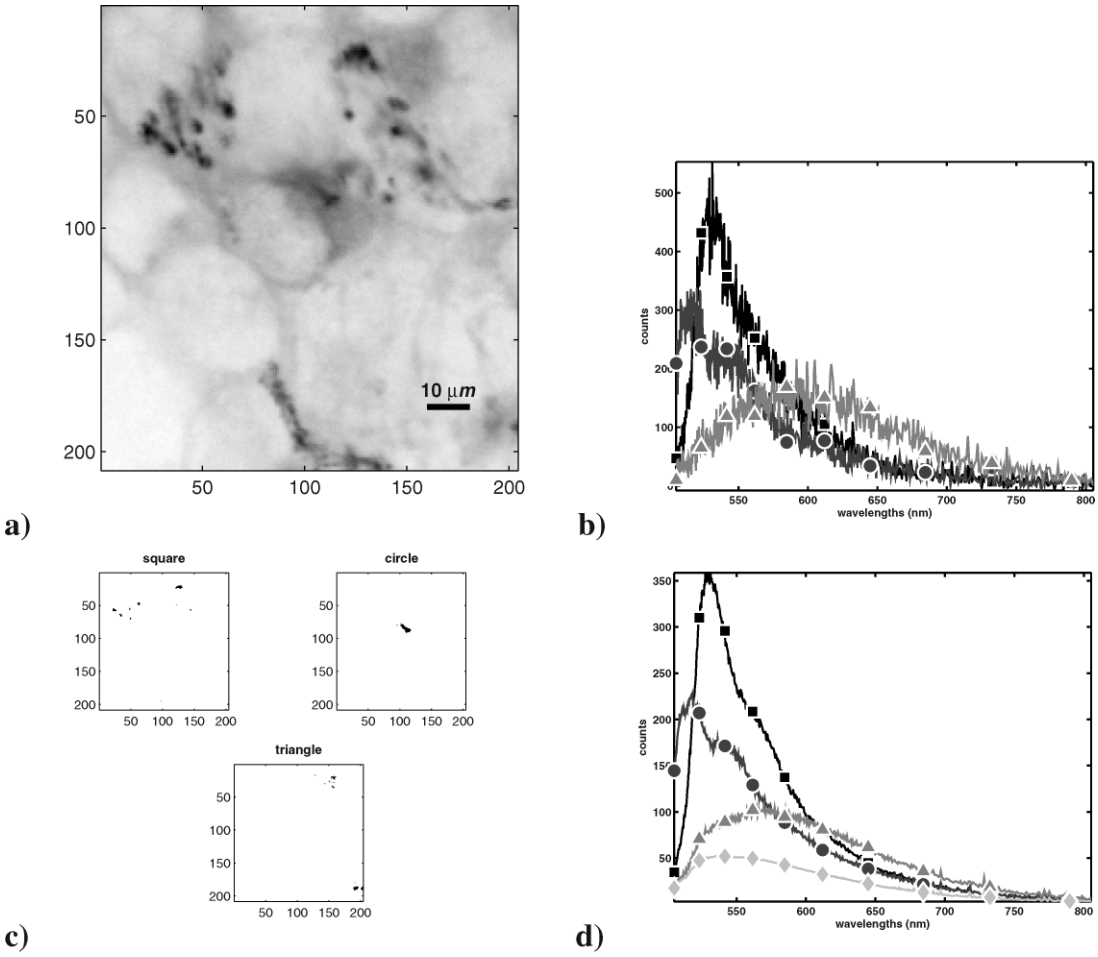

FIG. 3. Summary of compression of Image 1. (**a**) Integrated intensity representation of initial time slice (black represents high intensity). (**b**) Maximally dissimilar spectra in the image. (**c**) Maximally dissimilar regions with titles corresponding to the symbol representing the maximally dissimilar spectra in (b). (**d**) Initial spectra for all super pixels including an additional super pixel corresponding to the average of all pixels above the threshold but not included in the maximally dissimilar regions (diamond symbols).

analysis with PCA, it was determined that three fluorophores GFP, YFP, and autofluorescence (Auto) were present in both experimental images. In an initial investigation of the experimental images, it was apparent that kinetic modeling with a single first-order decay describing each fluorophore was not adequate. Investigations into the photostability of fluorophores are discussed in the literature, and it is common to use multiple exponentials to describe the photobleaching process[22–25] including that of fluorescent proteins.[26,27] Two proposed explanations for this observation are non-uniform illumination of the sample volume[28] and heterogeneity in the population of the fluorophore.[29,30]

In light of our initial observations and insights from the literature, we propose a more complex system of models in which each fluorophore is present in several different environments within the image. The presence of each fluorophore in different environments could cause multiple first-order kinetic photobleaching rates without affecting the spectral emission shape of the fluorophore. Building on this assumption, multiple different models were tested with each fluorophore described by up to three different local environments. The most complex model is shown in Fig. 1. For example, YFP is observed in environments YFP_1, which photobleaches to $YFP_{b(1)}$, YFP_2, which photobleaches at a different rate to $YFP_{b(2)}$, and YFP_0, which experiences negligible photobleaching during the exposure time of the experiment. A minimum of one first-order decay (YFP_1, GFP_1, and $Auto_1$) is necessary to describe each fluorophore, giving 8 possible combinations of secondary first-order decay species (YFP_2, GFP_2, and $Auto_2$) and 8 possible combinations of photobleach resistant species (YFP_0, GFP_0, and $Auto_0$), or $8 \times 8 = 64$ total combinations.

A major challenge in the kinetic modeling of these complex images is selecting the most parsimonious statistically sufficient mechanism. Due to the heteroscedastic noise structure in hyperspectral confocal images, analysis of spectral residuals in the training and test sets is not useful in model selection. Segmented cross-validation[31] also fails to provide useful insights. A methodical approach to selecting the best mechanism is implemented in this work. All 64 plausible mechanisms are fit to the compressed image data. Typically, many of the proposed mechanisms fit the data equally well, resulting in several statistically sufficient models. Due to inconsistencies with well-known characteristics of pure-component fluorescence spectra, many of the mechanisms can be discarded. For example, fluorescence spectra are not expected to exhibit multiple peaks in the emission band. In addition we know the approximate spectral emission shapes of

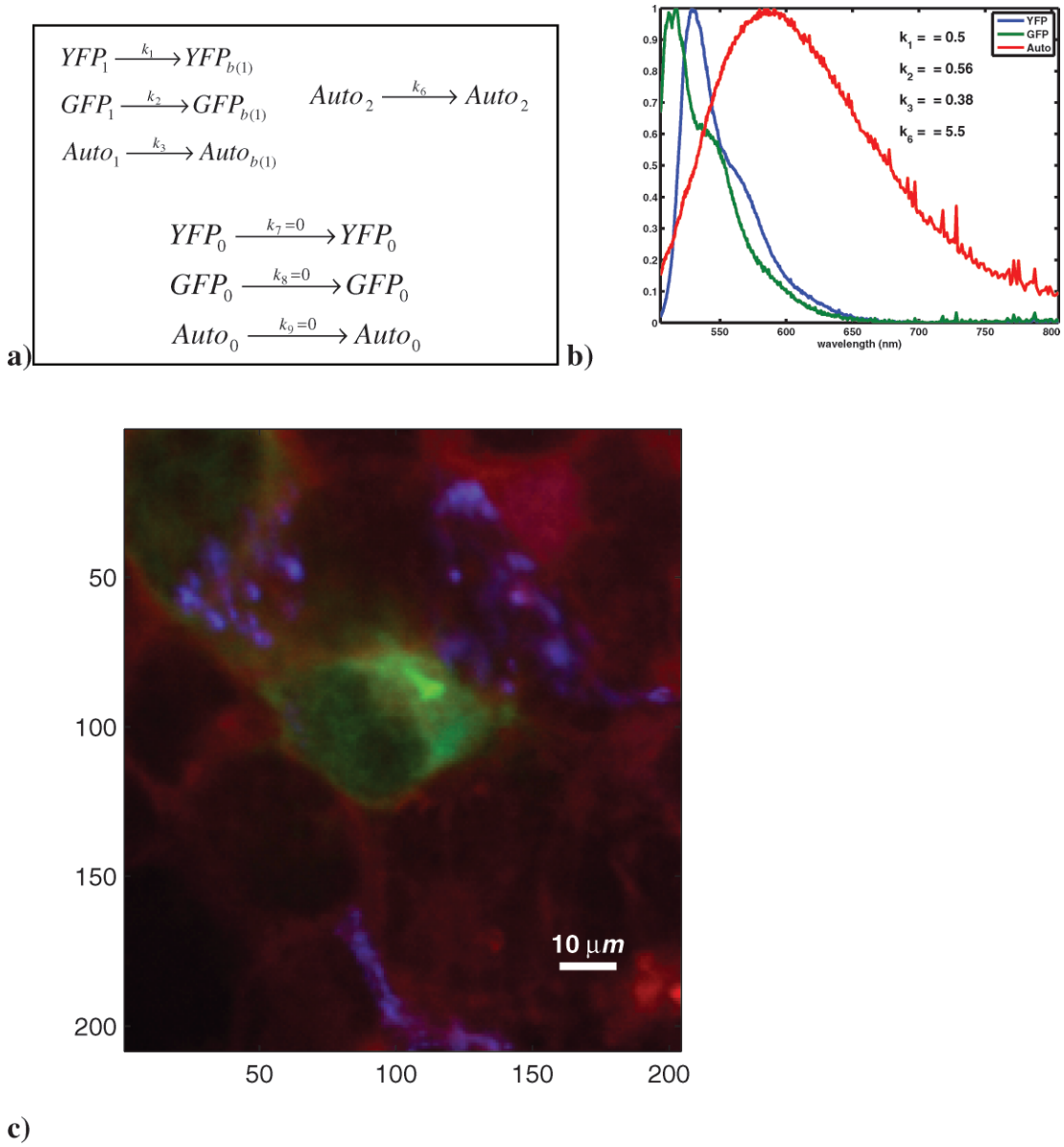

FIG. 4. Most parsimonious and statistically sufficient mechanism (**a**) and corresponding pure-component spectra (**b**) from kinetic modeling of Image 1. Spatial concentration maps for the initial time slice (**c**) from the extrapolation of the kinetic model to the full image. YFP, GFP, and Auto are represented by blue, green, and red, respectively.

the GFP, YFP, and autofluorescence from the literature, and the estimated pure-component spectra should resemble these emission shapes from the literature. Thus, these properties of the emission spectra can aid in the selection of the most appropriate kinetic mechanisms. In addition, the physical relevance of each model can be determined by inspecting the rate constants. Mechanisms resulting in very fast rate constants (greater than 10) are discarded because they are not observable on the time scale of these experiments. Mechanisms resulting in negative rate constants are discarded as well. Additional kinetic modeling of the mechanisms that provide physically relevant pure-component spectra and rate constants were performed with 10 random initializations. The standard deviation in the model parameters from several random initializations is used to determine how well the model parameters are defined. The simplest mechanism with consistently well-defined parameters (smaller standard deviations) and residuals at the noise level in the data is considered to be the most parsimonious and statistically sufficient model.

Once a mechanism is selected, the kinetic model of the compressed image is used to estimate the concentration map of the full image by extrapolation. The estimated pure-component spectra and rate constants are used in Eqs. 7, 8, and 11 to estimate the concentrations at t_0 for the full image. The estimated concentrations at t_0 are then used to estimate the concentration profiles for each pixel in the full image.

Kinetic Modeling of a Simulated Image. It is important to test our systematic kinetic modeling approach using an image with a known kinetic mechanism and known parameter values to demonstrate its usefulness. Therefore, the simulated image was analyzed using the systematic approach developed in this investigation. The preprocessing steps were not necessary for this image since the spectral image was generated from data that were already preprocessed. The image was compressed to

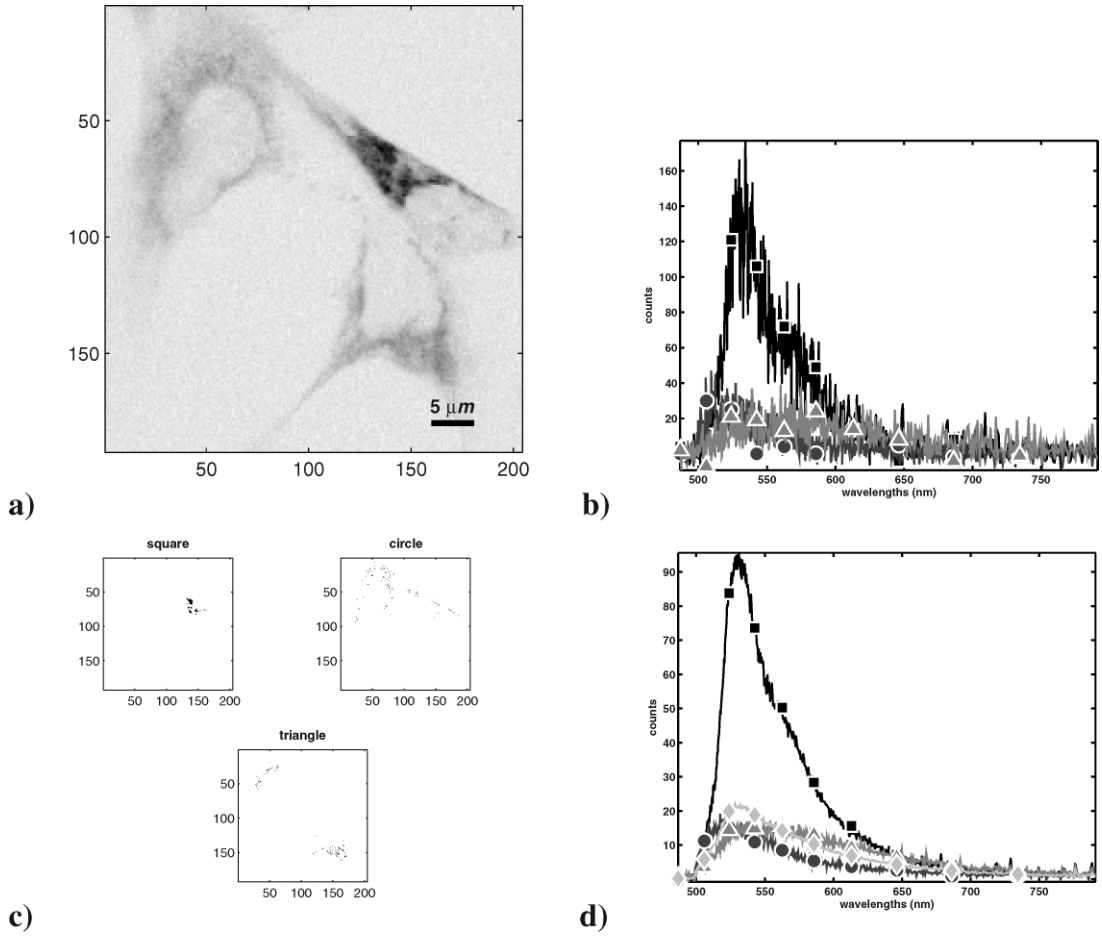

FIG. 5. Summary of compression of Image 2. (**a**) Integrated intensity representation of initial time slice (black represents high intensity). (**b**) Maximally dissimilar spectra in the image. (**c**) Maximally dissimilar regions with titles corresponding to the symbol representing the maximally dissimilar spectra in (**b**). (**d**) Initial spectra for all super pixels including an additional super pixel corresponding to the average of all pixels above the threshold but not included in the maximally dissimilar regions (diamond symbols).

four super pixels composed of three maximally dissimilar regions and an average of all other pixels above the threshold.

The compressed image was analyzed with all 64 possible models selected from the presence or absence of the Environment 2 and Environment 3 reactions summarized in Fig. 1. The two most physically relevant models are represented in Figs. 2a and 2b. The resolved pure-component spectra and estimated rate constants corresponding to Figs. 2a and 2b are presented in Figs. 2c and 2d. The mechanisms are nearly identical (i.e., rate k_1 is nearly 0, which is equivalent to a YFP_0 specie that does not photobleach in the time of the experimental measurement). The models were randomly initialized 10 times and the model in Fig. 2b was found to have the most well-defined model parameters (i.e., smallest standard deviation). Compared to the model shown in Fig. 2a, the model shown in Fig. 2b is simpler and thus more parsimonious. The model in Fig. 2b corresponds to the true underlying model used in generating the simulated data set. The strategies used for selecting the best model in Fig. 2 are used throughout the rest of this paper.

For the simulated data, the lack of fit for the model-estimated pure-component spectra relative to truth is 0.4%, 0.4%, and 0.3% for YFP, GFP, and Auto, respectively. A comparison of the model estimated rate constants to truth is included in Table I. The pure-component spectra and rate constants from kinetic

TABLE I. Comparison of true (actual) and estimated rate constants from the kinetic modeling of the simulated image and % Error from Eq. 20.

Rate constant	Actual	Estimated	% Error
k_1	0.52	0.52	0.2
k_2	0.54	0.54	0.1
k_3	0.41	0.41	1.0
k_4	6.62	7.32	10.5

TABLE II. Comparison of true (actual) and model estimated concentrations at t_0 from the kinetic modeling of the simulated image.

	Actual				Absolute deviation	
Species	Mean	Median	Min	Max	Mean	Median
YFP_1	19.5	10.4	0.0	332.1	1.5	1.1
GFP_1	14.2	6.4	0.0	238.1	1.1	0.8
$Auto_1$	18.2	17.5	0.0	73.6	0.8	0.7
YFP_0	1.8	0.2	0.0	52.5	0.4	0.2
GFP_0	3.1	1.2	0.0	42.3	0.4	0.3
$Auto_0$	13.5	12.8	2.4	74.9	0.4	0.3
$Auto_2$	3.5	3.1	0.0	25.3	0.8	0.6

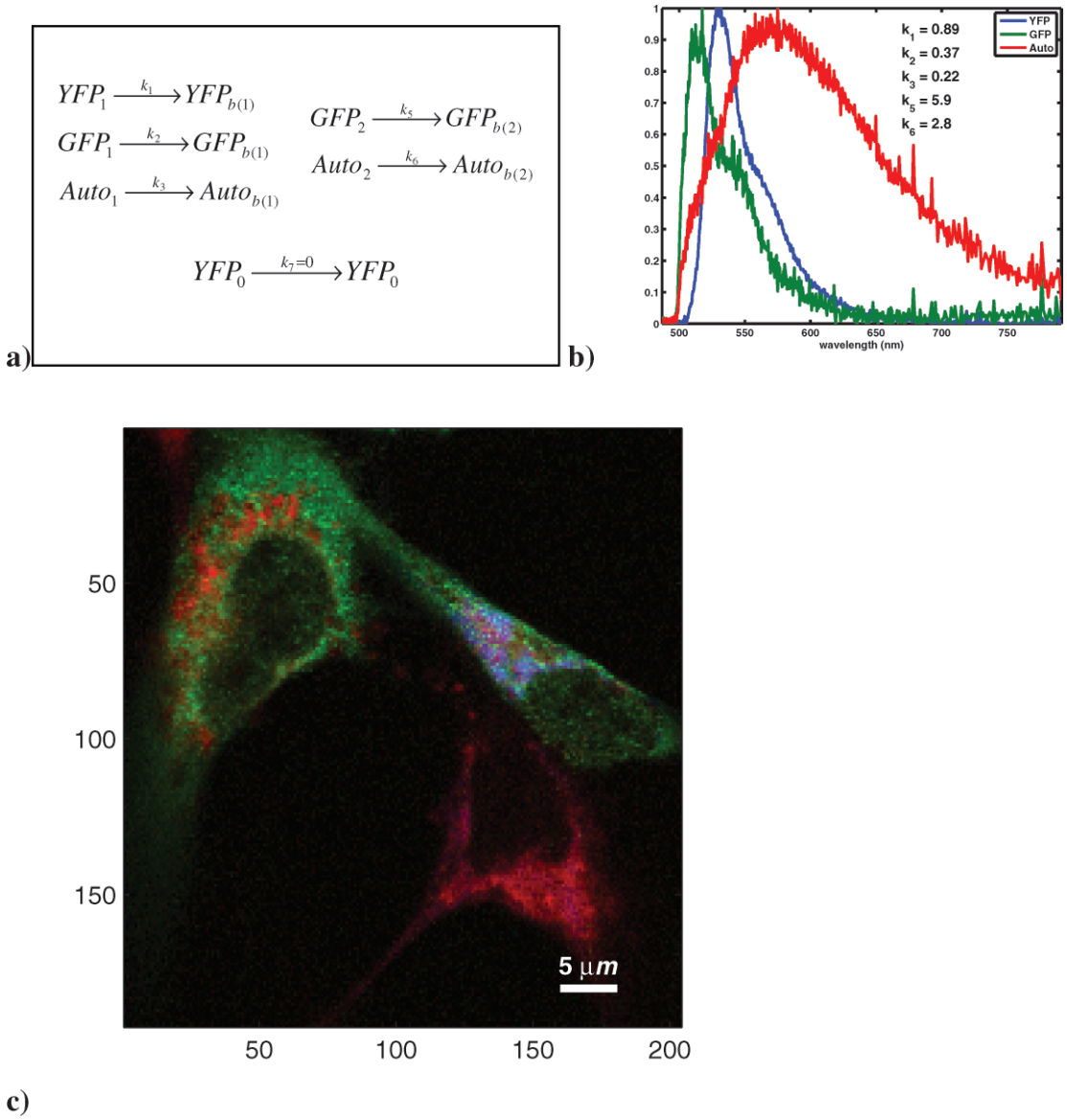

FIG. 6. Most parsimonious and statistically sufficient mechanism (**a**) and corresponding pure-component spectra (**b**) from kinetic modeling of Image 1. Spatial concentration maps for the initial time slice (**c**) from the extrapolation of the kinetic model to the full image. YFP, GFP, and Auto are represented by blue, green, and red, respectively.

modeling of the compressed image were used to estimate the concentration profiles for the full image. A summary of the actual concentrations for the full image at t_0 as well as a summary of the deviations of the estimated concentrations are shown in Table II. All figures of merit demonstrate that the model-estimated parameters are accurate.

Kinetic Modeling of Image 1. The spectral image was preprocessed as described previously, and an integrated intensity representation of the image is included in Fig. 3a. The image thresholding excluded less than 1% of the pixels in the image. Three maximally dissimilar spectra (shown in Fig. 3b) and subsequently three maximally dissimilar spatial regions were formulated. The maximally dissimilar regions and all other pixels above the threshold were averaged into four super pixels. The maximally dissimilar regions and corresponding representative spectra (spectra from the first time slice) are shown in Figs. 3c and 3d, respectively. A representative spectrum for the fourth super pixel is also included in Fig. 3d.

The compressed image was kinetically modeled using all 64 plausible reaction mechanisms from the set of reaction mechanisms that could be formulated from various combinations of reactions that are summarized in Fig. 1. The mechanisms that were selected to be the most physically relevant were randomly initialized 10 times. The mechanism presented in Fig. 4a was selected to be the most parsimonious and statistically sufficient mechanism. This model provided estimated spectra consistent with known pure-component spectra and residuals at the noise level in the data. The resulting pure-component spectra and rate constants are presented in Fig. 4b and were used to estimate concentration profiles for the full image. The resulting spatial concentration maps for the initial time slice are shown in Figs. 4c.

Kinetic Modeling of Image 2. An integrated intensity representation of the image is shown in Fig. 5a. The usual preprocessing steps were performed prior to data compression. Three maximally dissimilar spectra were selected and are

shown in Fig. 5b. The corresponding maximally dissimilar regions (shown in Fig. 5c) and all other pixels above the threshold were averaged into four super pixels. The spectra from the initial time slice for all super pixels are shown in Fig. 5d.

The super pixels were again kinetically modeled using the 64 mechanisms selected from the set summarized in Fig. 1. Several of the plausible mechanisms resulted in physically relevant rate constants and pure-component spectra. Each mechanism with physically relevant results was randomly initialized 10 times. The mechanism in Fig. 6a was determined to be the most parsimonious and statistically sufficient mechanism. This model provided estimated spectra consistent with known pure-component spectra and residuals at the noise level in the data. The resulting rate constants and pure-component spectra presented in Fig. 6b were used to estimate concentration profiles for the full image, and the resultant spatial concentration maps for the initial time slice is shown in Fig. 6c.

CONCLUSION

In this investigation, a systematic procedure for performing kinetic modeling on temporally resolved hyperspectral images was developed and applied to a simulated image and two experimental images. The physical phenomenon of photobleaching has been modeled in these images. In order to properly model the photobleaching kinetics, it was essential to compress the data. The initial step in data compression required the introduction of the selection of a set of maximally dissimilar spectra through a method based on the concepts originally developed for iterative key set factor analysis.[14] This technique helped retain a maximal amount of useful information during data compression. An extension of a previously presented separable least squares modeling procedure was implemented here and used to kinetically model hyperspectral image data with complex first-order kinetic mechanisms. It was observed that some mechanisms are mathematically indistinguishable or very similar. Due to the nature of the Poisson noise in hyperspectral microscope images, a major challenge in this work was selecting the most parsimonious and statistically sufficient mechanism. To that end a method to evaluate the pure-component emission spectra and to compare how well the mechanistic parameters are defined was developed.

The kinetic modeling performed in this research has provided us with new insights into the kinetic mechanisms of photobleaching. We initially assumed that each fluorophore might be represented as a single exponential decay. However, our kinetic modeling of the hyperspectral images led us to the conclusion that fluorophore photobleaching kinetics are significantly more complex than a simple exponential decay. In fact, our kinetic modeling of the temporally resolved hyperspectral images during photobleaching demonstrated that several first-order decays were often needed for each fluorophore to adequately model the data presented in this work. In addition, the kinetic fitting was consistent with a portion of the fluorescence not being subject to photobleaching within the time scale of the experiments. These kinetic results have led us to the hypothesis that different decay curves for each fluorescent specie are due to the presence of the fluorophore in different environments within the sample. Thus, a spatial map of each fluorophore in the various environments is obtained directly from the kinetic modeling process. It would be useful in a future experiment to investigate a system with a single fluorophore in several different spatially distinct environments. That experiment would help test our hypothesis of using mechanisms with several first-order decays to describe the photobleach kinetics of a single fluorophore.

ACKNOWLEDGMENTS

The authors would like to thank Howland Jones for software and data analysis support on this project and for preparing the simulated hyperspectral image data. Jens Poschet is acknowledged for preparing the fluorescently labeled A549 cells. Rachel Noek and Ryan Davis collected the hyperspectral data of the fixed cells. Allen Brasier from the University of Texas Medical Branch prepared the fluorescently labeled HEK 293 cells. Sandia is a multiprogram laboratory operated by Sandia Corporation, a Lockheed Martin Company, for the United States Department of Energy under Contract DE-ACO4-94AL85000. Support is acknowledged from Sandia National Laboratories' Laboratory Directed Research and Development project titled Microscale Immune Studies Laboratory (MISL).

1. X. Michalet, A. N. Kapanidis, T. Laurence, F. Pinaud, S. Doose, M. Pflughoefft, and S. Weiss, Annu. Rev. Biophys. Biomol. Struct. **32,** 161 (2003).
2. F. S. Wouters, Contemporary Phys. **47,** 239 (2006).
3. M. B. Sinclair, D. M. Haaland, J. A. Timlin, and H. D. T. Jones, Appl. Opt. **45,** 6283 (2006).
4. D. M. Haaland, M. B. Sinclair, H. D. T. Jones, J. A. Timlin, L. T. Nieman, G. D. Bachand, D. Y. Sasaki, G. S. Davidson, and M. H. V. Benthem, "3D Optical Sectioning with a New Hyperspectral Confocal Fluorescence Imaging System", in *Sandia Report* (Sandia National Laboratories, Albuquerque, NM, Livermore, California, 2007).
5. W. F. J. Vermaas, J. A. Timlin, H. D. T. Jones, M. B. Sinclair, L. T. Nieman, S. W. Hamad, D. K. Melgaard, and D. M. Haaland, Proc. Natl. Acad. Sci. U.S.A. **105,** 4050 (2008).
6. J. Zhang, R. E. Campbell, A. Y. Ting, and R. Y. Tsien, Natl. Rev. Mol. Cell Biol. **3,** 906 (2002).
7. S. Bijlsma, H. F. M. Boelens, H. C. J. Hoefsloot, and A. K. Smilde, Anal. Chim. Acta **419,** 197 (2000).
8. S. Norman and M. Maeder, Crit. Rev. Anal. Chem. **36,** 199 (2006).
9. G. Puxty, M. Maeder, and K. Hungerbuhler, Chemom. Intell. Lab. Syst. **81,** 149 (2006).
10. P. J. Cutler, D. M. Haaland, E. Andreis, and P. J. Gemperline, Appl. Spectrosc. **63,** 153 (2009).
11. M. Ehly, P. J. Gemperline, A. Nordon, D. Littlejohn, J. K. Basford, and M. De Cecco, Anal. Chim. Acta **595,** 80 (2007).
12. E. Furusjo, O. Svensson, and L.-G. Danielsson, Chemom. Intell. Lab. Syst. **66,** 1 (2003).
13. P. Gemperline, G. Puxty, M. Maeder, D. Walker, F. Tarczynski, and M. Bosserman, Anal. Chem. **76,** 2575 (2004).
14. K. J. Schostack and E. R. Malinowski, Chemom. Intell. Lab. Syst. **6,** 21 (1989).
15. P. Marchand and L. Marmet, Rev. Sci. Instrum. **54,** 1034 (1983).
16. E. R. Malinowski, Anal. Chim. Acta **134,** 129 (1982).
17. P. Gemperline, "Principal Component Analysis", in *Practical Guide to Chemometrics,* P. Gemperline, Ed. (CRC Press, Boca Raton, FL, 2006), p. 69.
18. M. H. Van Benthem and M. R. Keenan, J. Chemom. **18,** 441 (2004).
19. "Lipofectamine 2000 Manual" (Invitrogen, 2006).
20. "Nucleofector Manual 1.2" (Amaxa GmbH, November 2002).
21. H. D. T. Jones, D. M. Haaland, M. B. Sinclair, D. K. Melgaard, M. H. V. Benthem, and M. C. Pedroso, J. Chemom. **22,** 482 (2008).
22. C. Eggeling, L. Brand, and C. A. M. Seidel, Bioimaging **5,** 105 (1997).
23. C. Eggeling, J. Widengren, R. Rigler, and C. A. M. Seidel, Anal. Chem. **70,** 2651 (1998).
24. D. S. Ko, J. Chem. Phys. **120,** 2530 (2004).
25. X. S. Xie and J. K. Trautman, Annu. Rev. Phys. Chem. **49,** 441 (1998).
26. G. Patterson, Microsc. Microanal. **13,** Supplement S02, 294 (2007).
27. N. C. Shaner, R. E. Campbell, P. A. Steinbach, B. N. G. Giepmans, A. E. Palmer, and R. Y. Tsien, Nat. Biotechnol. **22,** 1567 (2004).
28. A. J. Berglund, J. Chem. Phys. **121,** 2899 (2004).
29. A. Molski, J. Chem. Phys. **114,** 1142 (2001).
30. A. Renn, J. Seelig, and V. Sandoghdar, Mol. Phys. **104,** 409 (2006).
31. H. Pedersen, L. Munck, and S. Engelsen, J. Am. Oil Chem. Soc. **77,** 1069 (2000).